ADVANCED FUNCTIONAL MATERIALS
www.afm-journal.de

Direct Ink Write 3D Printing of Fully Dense and Functionally Graded Liquid Metal Elastomer Foams

Spencer Pak, Michael D. Bartlett, and Eric J. Markvicka**

Liquid metal (LM) elastomer composites offer promising potential in soft robotics, wearable electronics, and human-machine interfaces. Direct ink write (DIW) 3D printing offers a versatile manufacturing technique capable of precise control over LM microstructures, yet challenges such as interfilament void formation in multilayer structures impact material performance. Here, a DIW strategy is introduced to control both LM microstructure and material architecture. Investigating three key process parameters–nozzle height, extrusion rate, and nondimensionalized nozzle velocity–it is found that nozzle height and velocity predominantly influence filament geometry. The nozzle height primarily dictates the aspect ratio of the filament and the formation of voids. A threshold print height based on filament geometry is identified; below the height, significant surface roughness occurs, and above the ink fractures, which facilitates the creation of porous structures with tunable stiffness and programmable LM microstructure. These porous architectures exhibit reduced density and enhanced thermal conductivity compared to cast samples. When used as a dielectric in a soft capacitive sensor, they display high sensitivity (gauge factor = 9.0), as permittivity increases with compressive strain. These results demonstrate the capability to simultaneously manipulate LM microstructure and geometric architecture in LM elastomer composites through precise control of print parameters, while maintaining geometric fidelity in the printed design.

1. Introduction

Direct ink writing (DIW) is a versatile additive manufacturing method. It enables the fabrication of intricate structures by extrusion of high-viscosity fluids through a fine nozzle to create fully dense and porous solids, high aspect ratio structures, and spanning elements for diverse fields including soft robotics, stretchable electronics, and biomedical applications.[1,2] The materials suitable for DIW span a diverse set of viscoelastic inks including highly loaded suspensions and emulsions, conductive pastes, and elastomers.[3–14] During DIW, the composition of the ink and the print processing parameters can be tailored to achieve precise control of filament microstructure across different length scales, which directly influences the properties of the printed object. Recently, shear-induced alignment has been demonstrated during printing of a variety of ink compositions and fillers such as liquid metal (LM) microdroplets,[3,4] liquid crystal molecules,[15–18] and high–aspect ratio fibers.[19,20] The alignment of the fillers follow the prescribed motion of the printer's nozzle, resulting in programmed anisotropic functional properties. For functional emulsion inks consisting of spherical LM microdroplets dispersed in a prepolymer matrix, both the ink properties and the printing process parameters are crucial for controlling LM microdroplet shape and orientation during DIW alignment.[3,4] The shear-induced alignment of LM microdroplets has been observed to occur at low $H^* = \frac{H}{\alpha D} \ll 1$, where H represents the programmed print height, α is the die-swelling ratio (greater than unity), and D is the nozzle diameter combined with conditions of high $V^* = V/C$, where V is the nozzle velocity

S. Pak, E. J. Markvicka
Mechanical & Materials Engineering
Smart Materials & Robotics Lab, University of Nebraska–Lincoln
Lincoln, NE 68588, USA
E-mail: eric.markvicka@unl.edu

M. D. Bartlett
Mechanical Engineering, Soft Materials and Structures Lab
Virginia Tech
Blacksburg, VA 24061, USA
E-mail: mbartlett@vt.edu

M. D. Bartlett
Macromolecules Innovation Institute
Virginia Tech
Blacksburg, VA 24061, USA

E. J. Markvicka
School of Computing
University of Nebraska–Lincoln
Lincoln, NE 68588, USA

E. J. Markvicka
Electrical & Computer Engineering
University of Nebraska–Lincoln
Lincoln, NE 68588, USA

The ORCID identification number(s) for the author(s) of this article can be found under https://doi.org/10.1002/adfm.202410908

DOI: 10.1002/adfm.202410908

and C is extrusion velocity. This approach is in contrast to most other DIW printing applications, where a single set of printing parameters is adopted, where both V^* and H^* are typically set to unity, to minimize the void content and ink deformation. These parameters are rarely adjusted during the printing process. For DIW printing of LM emulsions, the influence of the printing parameters on the dimensional accuracy and void content has not been examined. Regardless of application, surface quality, dimensional accuracy, and defect content are important factors that can directly impact the mechanical and functional properties of the printed structure.

The occurrence of voids within printed structures is a common issue in DIW. These unintended voids can arise from entrapment of air during the extrusion process, which can be influenced by the cross-sectional shape of the filament or ink fracture.[13,21–23] For LM emulsion inks, these void structures would impact functional properties such as thermal conductivity,[5,8,24–28] electrical conductivity,[29–34] dielectric permittivity,[35–37] and acoustic impedance[38] of the printed sample. While quality control of raw materials and finished products is well established, uncertainties remain regarding the quality of individual layers. Integrating inline or post-process monitoring with DIW could address these uncertainties by assessing process-specific manufacturing variations to enhance print quality and ultimately enable more accurate predictions of product performance.[13,39–41] To achieve optimal functionality of the printed structure, the relationship between print processing parameters, resulting void content, and material and structural properties must be systematically studied.

The intentional introduction of voids can also have a positive effect from a structural perspective. Voids can be utilized to decrease the density of a material and have a significant impact on the mechanical response. Conventionally, polymeric foams are manufactured using methods that involve foaming agents,[42–44] gas dissolution,[45–47] or sacrificial templates,[48–50] to produce complex 3D porous structures. However, achieving different porosities or functionally graded foams through these means often requires modifications to the material composition or template design. Recent advancements, including microfluidic techniques and direct bubble writing, offer promising approaches for controlling the structure and porosity of polymeric foams.[51–53] However, while these methods afford high tunability, they are limited to low-viscosity fluids. In addition, existing methods would result in primarily spherical LM microdroplets with limited control over LM microstructure due to insufficient shear stress generated from substrate interactions.

Here, we report a DIW additive manufacturing method for creating both fully dense solids and porous foams using high viscosity LM emulsion inks. This method enables the creation of printed structures with programmable porosity and control over LM droplet microstructure, both of which strongly governs functional properties, through a single nozzle and ink formulation. The functional emulsion ink consists of spherical LM microdroplets (200 µm diameter and 50% by volume) embedded within a high-viscosity silicone prepolymer matrix (ExSil 100, Gelest). After printing, the composite is cured into a soft and highly extensible elastomeric composite. In prior work, we have demonstrated the ability to control the printing process conditions to transform the initially spherical LM droplets into highly elongated and oriented ellipsoids in primarily individual filaments and single-layer structures.[3,4] Here, we investigate the impact of the non-dimensional nozzle speed (V^*), nozzle height (H), and extrusion rate (C) on the resultant filament geometry, including width, height, cross-sectional area, and aspect ratio (**Figure 1**). By analyzing the filament geometry, we identified optimal parameters for fabricating dense multilayered structures and high aspect ratio features with improved surface quality and minimal internal defects for any V^* and H. However, because of die swelling and ink spreading post-deposition, which depends on printing conditions, the programmed layer height and the resulting printed filament height are often different (Figure S1, Supporting Information). This discrepancy can result in increased surface roughness or the formation of voids. To address this, we adjust the programmed layer height based on the measured printed filament geometry to ensure the creation of high-quality multilayer structures while retaining control over the LM droplet microstructure. Under specific printing conditions, the printed filament can become discontinuous despite a continuous nozzle path. As nozzle speed and height increase, the extruded ink thins and eventually becomes unstable due to the Plateau-Rayleigh instability and poor adhesion to the substrate, resulting in discontinuous segments. We exploit this instability and fracture behavior of the viscoelastic emulsion ink to tailor the relative porosity of the structure and create functionally graded foam structures without modifying the ink formulation itself. This unique combination of DIW control and functional emulsion inks offers a rapid and versatile approach to control the microstructure and architecture of LM elastomer composites.

2. Results and Discussion

2.1. Direct Ink Write 3D Printing and Characterization

A mechanically driven syringe pump was used to extrude the LM emulsion ink from a syringe at a specified extrusion speed while the nozzle moved laterally along the substrate at a specified height (Figure 1a). As demonstrated in prior work, the shape and orientation of the LM microdroplets can be controlled by adjusting printing process parameters (V^*, H), as well as ink properties (LM droplet size and ink viscosity).[3,4] For this study, the LM emulsion ink was formulated with a high viscosity and large LM microdroplet size (200 µm diameter, 50% by volume) to promote the formation of elongated LM microdroplets with high aspect ratios. To investigate the effect of the printing process parameters V^*, H, and C on filament geometry, laser profilometry was performed to measure individual filament width, height, and cross-sectional area (Figure 1b). These measurements were utilized to create space-filling solids that were printed in a uniformly aligned pattern and composed of more than ten layers to investigate the effect of processing parameters on void formation and surface quality (Figure 1c).

During DIW 3D printing, alternating layers were partially cured using a heat gun (see the Experimental Section for details, Movie S1, Supporting Information). After printing, the surface quality of the samples was visually examined using optical microscopy, while the void content or porosity was analyzed using microfocused X-ray computed tomography (XCT, Figure 1d). Precise control of print process parameters during deposition is

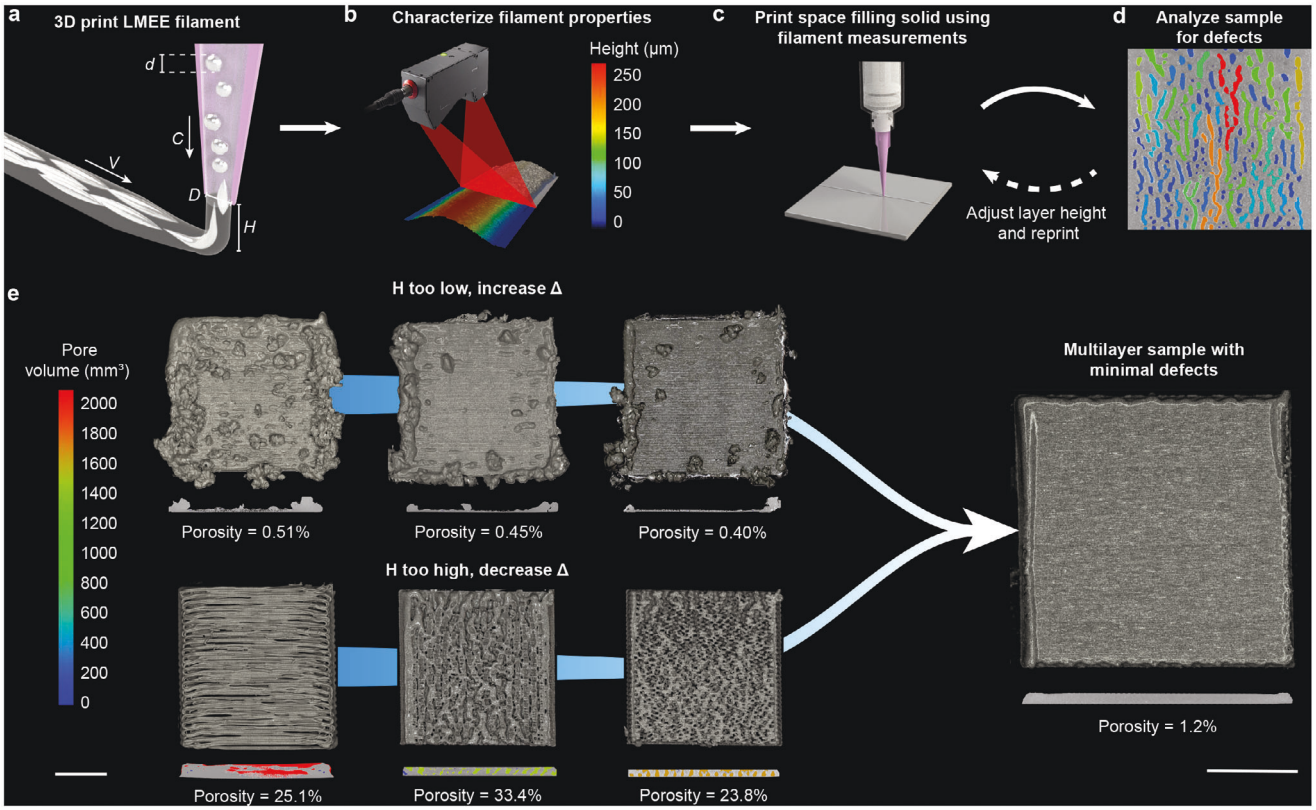

Figure 1. DIW printing to control geometric structure and LM microstructure. a) Schematic representation of the DIW printing process. As the ink is extruded through the nozzle, LM droplets can be elongated depending on V^* and H. b) Laser profilometry is utilized to characterize the filament geometry. c) These measurements are used to create multilayer structures. d) X-ray computed tomography is used to measure the porosity of the printed sample and assess quality. If necessary, the layer height is adjusted. e) Optical images of samples printed at extremely low and high H. By systematically controlling H, fully dense samples can be created with minimal defects. Scale bars 10 *mm*.

critical, as void formation and surface quality directly impact the mechanical and functional properties. As shown in Figure 1e, H can be systematically adjusted to achieve the desired external and internal print quality of the space-filling solid. Samples printed at a low H, as shown in the top row of Figure 1e, exhibited ink accumulation on the edges and surface, resulting in samples with a reduced overall height and high surface roughness. This is likely attributed to die-swelling,[54] where the extruded filament area exceeds the nozzle's area, which is common in viscoelastic inks. Conversely, printing at elevated H, as shown in the bottom row of Figure 1e, can yield structures with interfilament voids and high porosity due to ink spreading post-deposition and the formation of discontinuities at higher V^* and H. To address these challenges, an offset Δh is employed, where Δh is the difference between the measured filament height (H_f) and the programmed layer height ($\Delta h = H_f - H$, Figure S1, Supporting Information). The filament height was measured by laser profilometry prior to printing multilayered structures (Figure 1b). The programmed print height for multilayered structures is defined by $H \times L + \Delta h(L-1)$, where L is the layer being printed. As demonstrated in Figure 1e, the programmed layer height can be systematically adjusted to achieve the desired external and internal print quality of the space-filling solid, thereby enabling fabrication of multilayer structures with minimal defects at any given H and V^*.

2.2. Effect of DIW Printing Parameters on Filament Geometry

A Hyrel Engine SR printer with a mechanically driven print head was used to investigate variations in filament geometry as a function of process parameters (H, V^*, and C) as shown in **Figure 2**. The LM emulsion ink was printed at two different heights based on the critical nozzle height $H_c = \frac{\pi D}{4V^*}$, where D represents the diameter of the nozzle: i) a height $1.5 \times H_c$ above the critical height and ii) a height $0.9 \times H_c$ below the critical height.[55] Printing below the critical nozzle height will cause the filament to squeeze and expand outward, as the space between the nozzle and print bed is smaller than the volume of the extruded material, assuming volume conservation within a flat cuboid shape. Conversely, printing above the critical height, the filament will maintain a rounded shape during extrusion, with ink spreading occurring post-deposition. In addition, we also included a lower height of 200, 50, and 20 μm at $V^* = 1$, 6, and 12, respectively. These heights were based on previous work to achieve maximum LM microdroplet elongation.[3,4] V^* is also a key processing parameter that affects LM microstructure and filament geometry as shown in Figure 2a and Movie S2 (Supporting Information). The emulsion ink was printed at $V^* = 1$, 6, and 12, resulting in nine different combinations of H and V^*. To study the effect of extrusion rate C on trace formation, three different values were selected $C = 6.8$, 5.0, and 2.5 mm-s^{-1} for each H and V^*. The profile

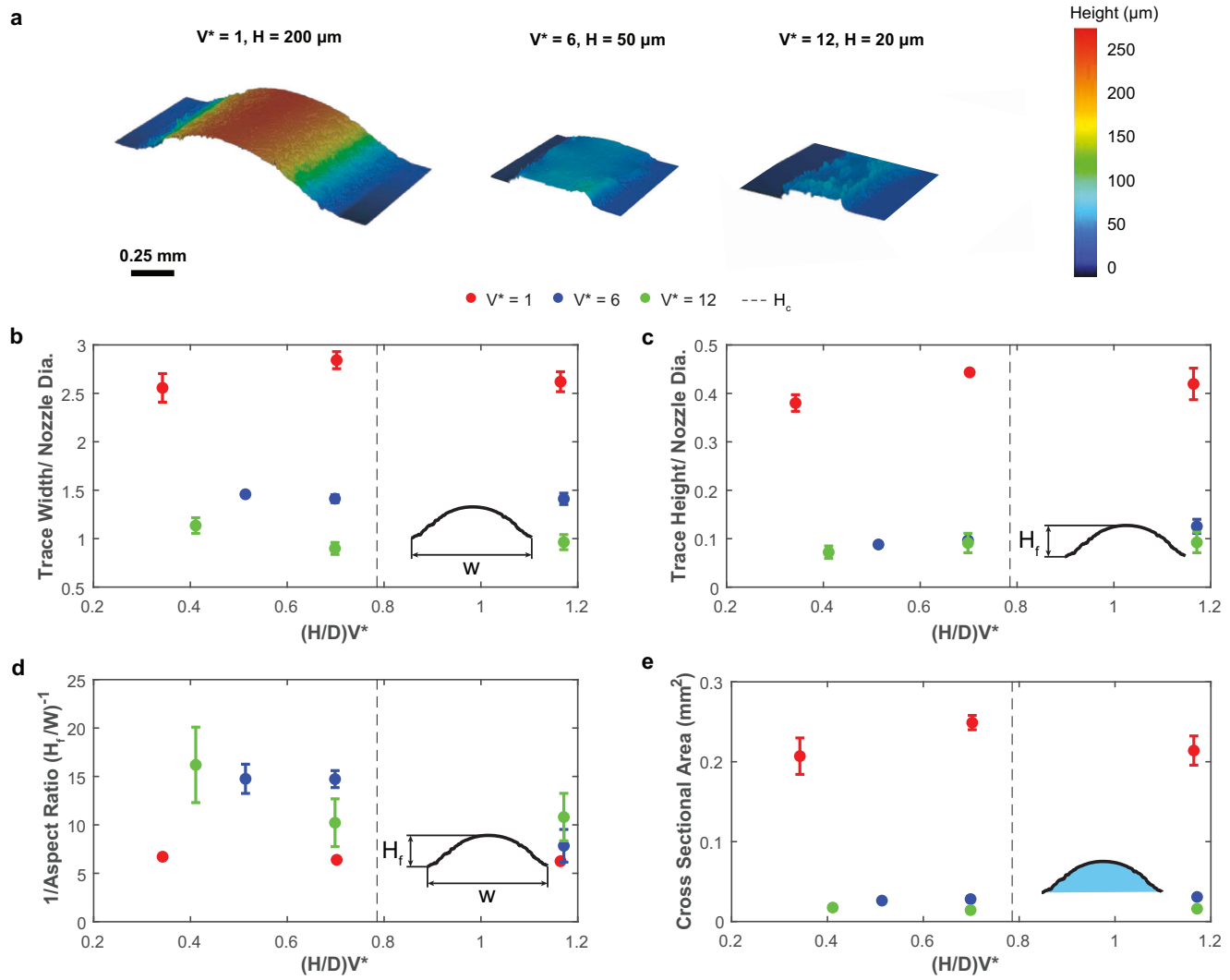

Figure 2. Filament characterization a) Laser profilometry models of filaments printed at $V^* = 1$, 6, and 12 and $C = 2.5$ mm-s^{-1}. The measured b) normalized width, c) normalized height, d) inverse aspect ratio $(H_f/W)^{-1}$, and e) cross-sectional area of individual filaments printed at $V^* = 1$, 6, and 12 vs. H. b,c) The y-axis is normalized by the nozzle diameter (580 µm). b–e) The x-axis is normalized by D/V^*, which is proportional to the critical printing height H_c. Data are presented as the mean ± s.d. ($n = 3$) for each combination of parameters.

of each filament was imaged using laser profilometry (Figure S2, Supporting Information).

The average filament width, normalized by the nozzle diameter, is observed to be similar for all H and C tested and mainly influenced by V^* due to the reduction of material being extruded per length (Figure 2b). The x-axis of Figure 2b–e is normalized by D/V^*, which is proportional to the critical printing height H_c (dashed black line). As V^* increases from 1 to 12, the normalized width of the filament ranges from 3× the nozzle diameter to just slightly less than the nozzle diameter. The data for all combinations of printing parameters are included in Figure S3 and Table S1 (Supporting Information). The average filament height, normalized by the nozzle diameter, generally decreases as H decreases and V^* increases (Figure 2c). There are negligible changes with respect to C (Figure S3, Supporting Information). On average, the filament height can be reduced by 30% for $V^* = 1$ and 6, with smaller reductions observed for $V^* = 12$. The largest reduction of up to 85% in height is observed as V^* is increased from 1 to 12. In general, we see that for these processing parameters and ink properties the extruded ink is compressed due to H and then further spreads post-deposition, which results in the width of the filament being much greater than the nozzle diameter. This relationship is illustrated by the average printed filament aspect ratio (H_f/W). To emphasize the correlation between filament width and height, the inverse aspect ratio is plotted in Figure 2d. The inverse average printed filament aspect ratio $(H_f/W)^{-1}$ increases as H decreases and V^* increases. There are negligible changes with respect to C (Figure S3, Supporting Information). The average cross-sectional area is observed to decrease with increasing V^*, which is expected and due to the reduction of material being extruded per length (Figure 2e). There are negligible changes with respect to H and C. The relationship between the predicted area and the measured area is shown in Figure S4 (Supporting Information). The comparison shows

good agreement, indicating that the assumption of volume conservation is reasonable. The extrusion rate used to calculate the predicted cross-sectional area was empirically measured by calculating the volume of material extruded in one minute. The measured extrusion rates were lower than those calculated as shown in Table S2 (Supporting Information). Assuming incompressibility and volume conservation of the extruded ink, the predicted area of the printed filament can be calculated as $A = \frac{\pi(D/2)^2}{V^*}$.

The cross-sectional geometry of the printed filament is greatly influenced by V^* and H (Figure 2). When H is low and V^* is high, a rectangular and wide filament shape is observed, whereas a bell shape is observed at high H and low V^*. At low H, the ink is pressed and forced to spread to the sides, resulting in high aspect ratios. At high V^*, the ink is stretched and thinned due to the high relative velocity between the print bed and the extruded ink, resulting in continuous but considerably smaller filaments compared to the nozzle area. However, depending on the combination of H and V^*, the printed filament will intermittently fracture, causing discontinuities. As shown in Figure S5 (Supporting Information), at a constant $V^* = 12$ the size and frequency of discontinuities increase with increasing H. In the printing regime studied here ($0.03 \leqslant H^* \leqslant 1.17$), H^* is considerably lower than conventional DIW 3D printing, where H^* is typically set to unity. This low H^* allows us to leverage substrate interactions, enabling simultaneous control over both the LM microstructure and geometric architecture.

2.3. Effect of Printing Parameters on Multilayered Structures and Void Formation

The control of printing parameters V^* and H are critical for tailoring the microstucture of embedded LM droplets. However, these parameters have a large influence on the resulting filament cross-sectional geometry as well. To examine their impact on the formation of interfilament voids and surface roughness, we created multilayered structures with extreme minimum and maximum H for $V^* = 1$, 6, and 12 (**Figure 3**a–c; Movie S3, Supporting Information). Unless otherwise noted, all multilayer structures were created with $C = 2.5$ mms^{-1} to ensure the nozzle velocity remained within the printer's recommended X/Y velocity and trace spacing was set to 75% of the measured trace width. For structures created with low H across all V^*, the ink was pressed and forced outwards, filling interfilament areas, which resulted in thin samples with minimal voids (Figure 3a–c (left column)). However, die swelling caused the nozzle to accumulate extrudate, leading to material build-up and increased surface roughness. In contrast, at high H, the ink was not able to adhere to the previous layer effectively resulting in thicker samples with significant void formation (Figure 3a–c (right column)). At $V^* = 1$, the printed filament remained continuous, but formed a meandering pattern that deviated from the nozzle path, creating large voids. Meandering patterns are commonly observed at low $V^* \leqslant 1$ and high $H > D = 580$ µm.[11,56,57] For higher V^* of 6 and 12 and lower $H \ll D$, the filament was stretched during deposition due to higher print speeds, leading to ink fracture, generating discontinuous filament segments.

To address these challenges and enable the fabrication of fully dense, high-quality multilayer structures for any given V^* and H, an offset Δh was applied to adjust the print height of each layer based on the measured filament height (Figure S6, Supporting Information). As demonstrated in Figure 3d–f, systematically adjusting H based on H_f can significantly reduce surface roughness and formation of interfilament voids in fully dense multilayer structures. This approach is effective regardless of the programmed H or V^* required to tailor the microstructure of the embedded LM droplets.

The LM droplet microstructure within multilayered structures was then analyzed using optical microscopy. Consistent with previous findings in single-layer structures, the shape and orientation of the LM droplets can be programmed by altering the print parameters V^* and H. At slower printing speeds, the droplets tend to remain spherical, similar to the emulsion ink. However, increasing V^* and decreasing H transforms the droplets from spherical to elongated, needle-like geometries. Importantly, this 3D printing strategy maintains control over the microstructure of LM droplets throughout the entire multilayer structure, even as the porosity of the structure varies (Figure 3g; Figure S7, Supporting Information). The porosity and pore size for each condition were measured using XCT and 3D image analysis, with the results shown in Figure 3h. This demonstration validates the proposed strategy for creating fully dense and porous solids with programmable LM microstructures, which ultimately governs functional properties such as thermal conductivity.

We then examined the effects of porosity on the thermal conductivity of printed multilayer structures. The thermal conductivity of two cast samples and two printed samples was measured using a transient plane source (TPS) method. The sensor was placed between two homogeneous samples, which functions as both a heat source and temperature sensor (Figure S8, Supporting Information). Two samples were cast with 0% and 50% volume loading of LM and their respective thermal conductivities were $k = 0.15$ and 1.45 Wm^{-1}·K^{-1}, consistent with previously reported values (Figure 3i; Figure S8, Supporting Information).[24,26] These samples were compared to two samples that were 3D printed at $V^* = 12$ and $H = 0.08$. We observed that when printed with the Δh offset, the sample had the highest thermal conductivity of $k = 3.3$ Wm^{-1}·K^{-1}. Additionally, the sample printed without the Δh offset, exhibited a reasonably high thermal conductivity of $k = 2.13$ Wm^{-1}·K^{-1}. This exceeded the thermal conductivity of the replica-molded sample with the same volume loading of LM, despite its considerably high porosity of over 30%. By simultaneously controlling the geometric structure and LM microstructure, the thermal conductivity was increased by nearly 50%, while reducing the density of the part by over 30%. This demonstration illustrates the ability to control not only the thermal conductivity but also the material structure through the DIW 3D printing method using a single emulsion ink and manufacturing system to optimize part-level properties.

2.4. Printing Structures with High Aspect Ratio

To further demonstrate the versatility of the DIW 3D printing process, we fabricated a series of self-supported, interdigitated millimeter-scale structures with high aspect ratios (**Figure 4**a). The interdigitated keys were printed at $V^* = 1$, 6, and 12 and $H = 0.25$, 0.045, and 0.05 mm. Printing at lower V^* tended to

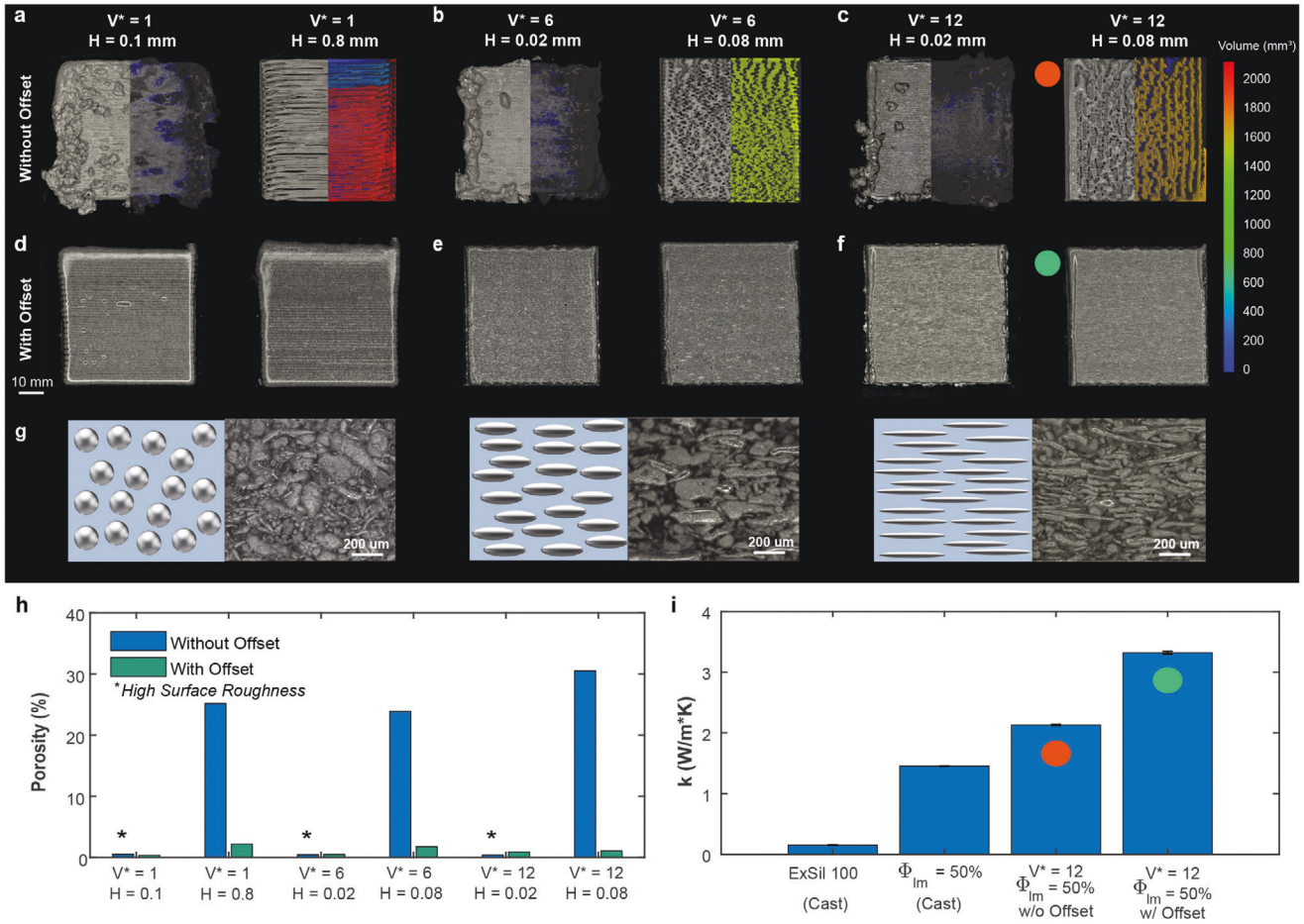

Figure 3. Characterization of multilayer samples. a–c) Optical microscopy images and corresponding XCT porosity analysis of multilayer samples printed at $V^* = 1$, 6, and 12 without offset Δh. Due to die swelling and ink spreading, the printed samples have several defects. Colorbar indicates pore volume. d–f) By utilizing the Δh offset to account for die swelling and ink spreading, fully dense structures can be created with minimal defects, independent of H and V^*. g) Schematic illustration and optical microscopy images of LM droplet microstructure of samples printed at $V^* = 1$, 6, and 12. h) At low values of H, the samples are observed to have high surface roughness. As H increases above the optimal value of H, the porosity is observed to increase. i) Comparison of thermal conductivity between pure elastomer and LM elastomer composites with 50% volume loading of LM. The printed samples, even with high porosity, have improved thermal conductivity as compared the cast samples. Data are presented as the mean ± s.d. ($n = 3$).

create keys with larger widths and lower aspect ratios (defined as key height/width) due to the low H and post-deposition spreading of the ink. Increasing V^* to 6 and 12, structures were created with sharper edges and more defined features. Due to the low H and spreading of the ink after deposition, the overall dimensions of the structures tended to be 1.2× to 1.6× larger than the expected key width, with a minimum lateral feature size of 1.25 mm (Figure 4b, c). The aspect ratios for the structures printed at $V^* = 1$, 6, and 12 measured 0.561, 1.540, and 2.176, respectively (Figure 4d). This demonstrates the ink's ability to reliably flow through the fine nozzle, robust adhesion between printed layers, and ability to withstand curing without distortion. Refinement of key width and aspect ratio could potentially be achieved by using a smaller nozzle diameter or increasing the number of printed layers. These intricately designed interdigitated structures could be used for various applications, such as heat sinks, soft capacitive strain sensors, or energy harvesting devices for applications such as soft robotics or wearable electronics.

2.5. Printing of Functionally Graded LM Elastomer Foams

The DIW 3D printing strategy enables novel functionalities beyond the limits of conventional DIW 3D printing. For example, the ability to print diverse complex patterns by using ink fracture would enable the creation of porous structures with tunable stiffness and programmable LM microstructure. While previous methods relied on a coiling instability with high-viscosity liquids to create porous structures,[11] they were constrained by the significantly high nozzle height relative to the diameter of the print nozzle ($H \gg D = 580$ µm). The high H would limit the precise control over the microstructure of the LM microdroplets, as there is no observable change in microstructure due to extrusion through the nozzle.[3,4] Here, we demonstrate that LM elastomer foams can be printed with tunable porosity in a reproducible and predictable manner through ink fracture (**Figure 5a**). The porous structures exhibit a disordered network formed by the stochastic creation of voids. These pores originate from filament discontinuities, which occur randomly but increase in size

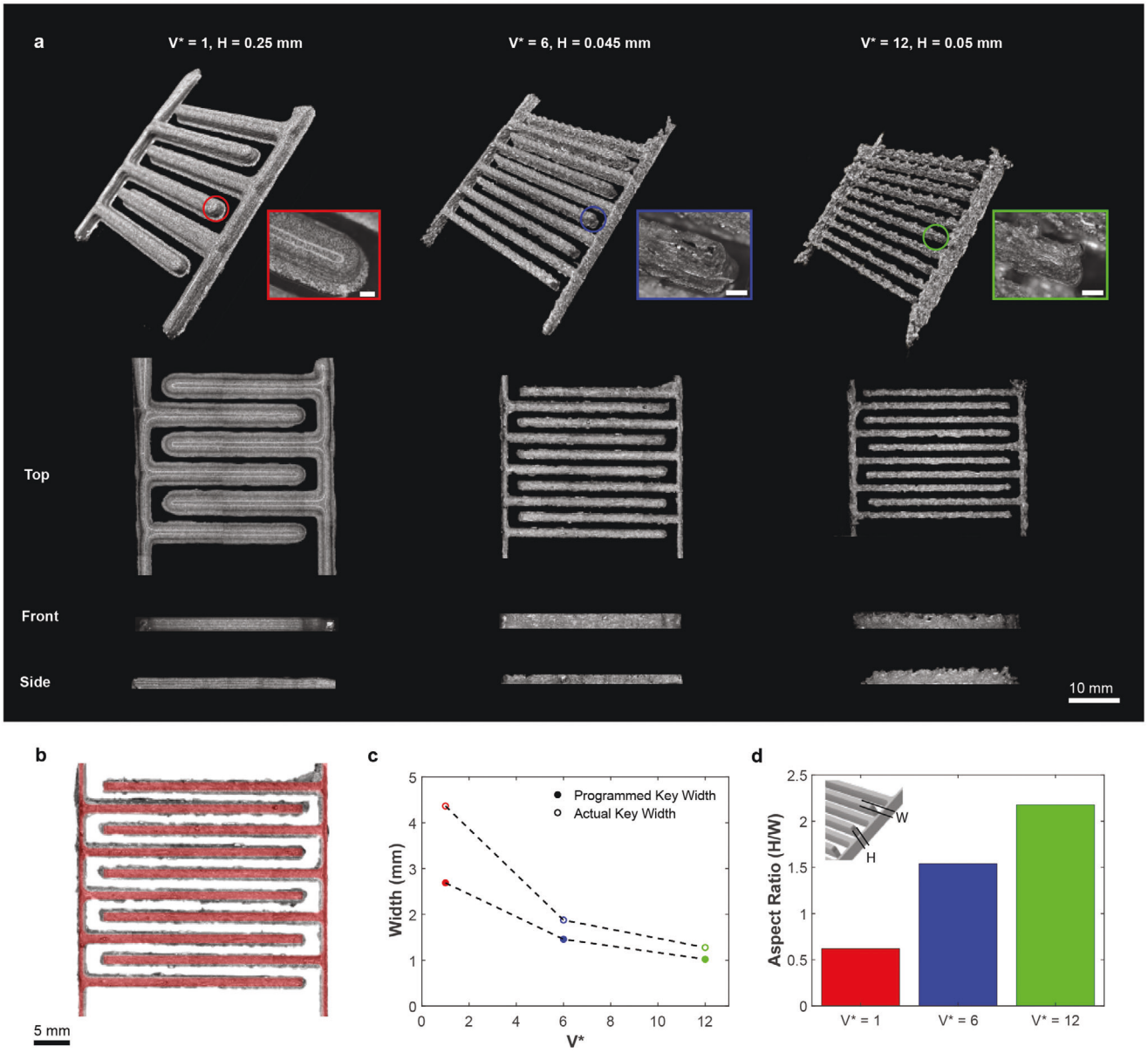

Figure 4. Printing high aspect ratio structures a) Optical microscopy images of interdigitated keys printed at V^* = 1, 6, and 12. Inset: Zoomed in image of individual keys. Scale bar 500 µm. b) Comparison of expected (red) versus measured structure geometry for V^* = 6. c) The measured key width is larger than the expected key width for all V^* due to the low H and ink spreading. d) Measured aspect ratio (key height/width) as a function of V^*.

and frequency with increasing H (Figure S5, Supporting Information). The porosity of the LM elastomer composite was controlled by increasing H above the optimal value where $\Delta h = 0$. As H increased at $V^* = 12$ without adjusting Δh, the porosity increased from 0% to 30%, with a standard deviation of less than 6% (Figure 5b). Importantly, even as H was increased above the optimal value, we maintained control over the microstructure of the LM microdroplets (Figure 5c). This process can also be used to create functionally graded LM elastomer foams. As shown in Figure 5d, the gradient structure was varied through the thickness by increasing H every 15 layers. By increasing H from 50 to 70 µm in increments of 10 µm, we achieved a porosity gradient spanning from 2.1% up to 51.3% (Figure S9, Supporting Information). This versatility enables tailoring of both the material properties and structure by controlling the print process parameters.

The functionally graded LM elastomer foam can be utilized to create a soft capacitive strain sensor by placing the dielectric foam between two electrodes. A functionally graded LM elastomer foam composite was created with a highly porous and nonporous section in a single print. To create a fully dense region, the sample was printed at $V^* = 12$ and an optimal $H = 50$ µm for 30 layers. Next, to create a highly porous region, H was increased to 70 µm ($\Delta h = 0$). The electromechanical response of the sensor was characterized by performing cyclic loading at increasing levels of strain, from 10%, 20%, 30%, 40%, and 50%. After an initial

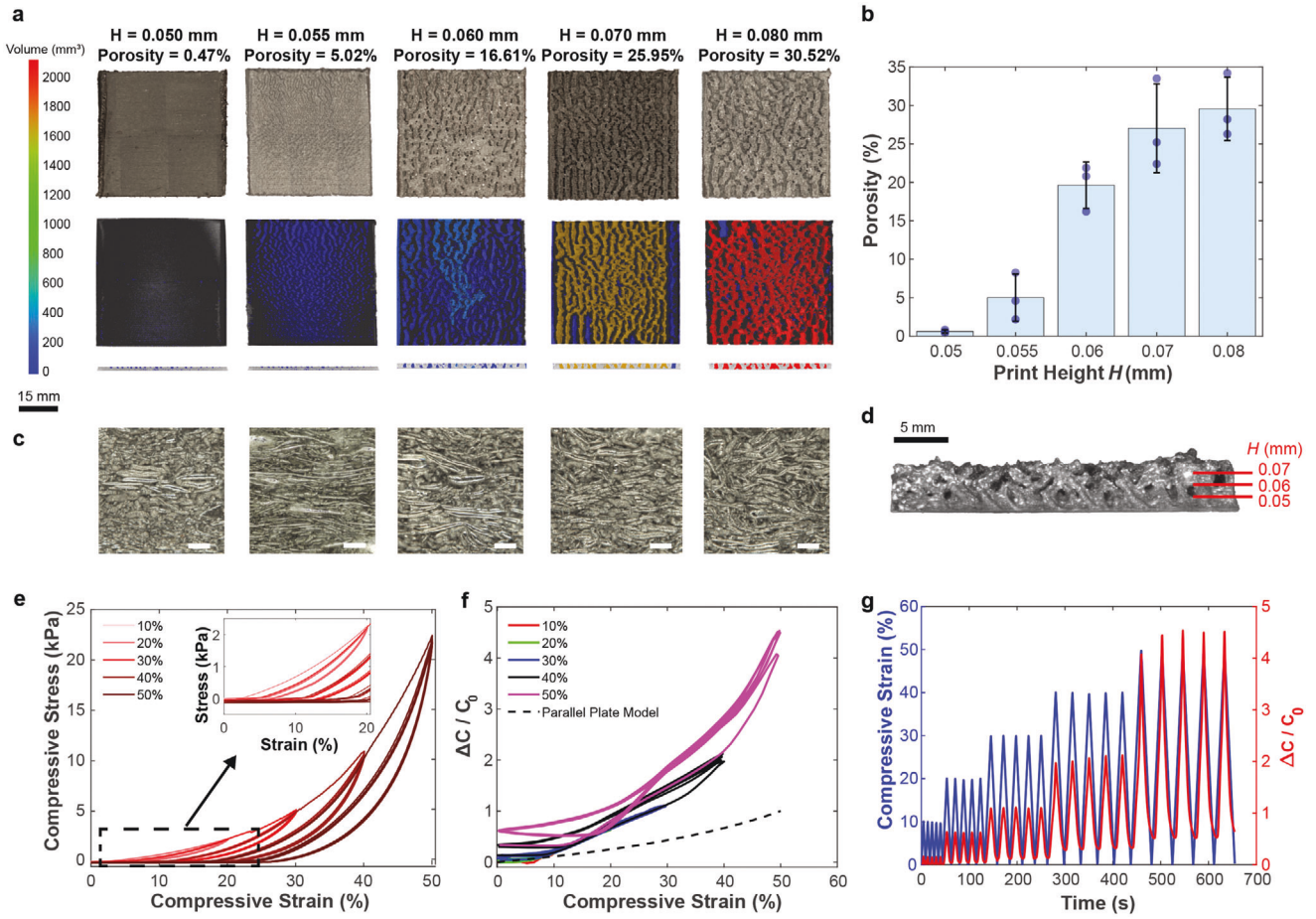

Figure 5. Characterization of functionally graded LM elastomer foam a) Photographs (top row) and XCT scans (bottom row) of V^* = 12 multilayer samples printed at increasing heights H = 50, 60, 70, and 80 µm. Colorbar indicates pore volume. b) The porosity of the samples can be tailored by changing the print height (H), where Δh is not used. Data are presented as the mean ± s.d. (n = 3). c) Optical microscopy images of LM microstructure in multilayer porous structures printed at V^* = 12 and H = 50, 60, 70, and 80 µm. Scale bars 200 µm. d) A cross-section photograph of the functionally graded LM elastomer foam. The sample was printed at V^* = 12 and H was increased from 50 to 70 μm, resulting in increased porosity. e) Cyclic loading of graded LM elastomer foam to increasing strains (10%, 20%, 30%, 40%, and 50%). f) Cyclic loading of capacitive sensor to increasing strains (10%, 20%, 30%, 40%, and 50%). Normalized change in capacitance plotted as a function of strain. g) The mechanical (blue) and electrical (red) response of the capacitive sensor to increasing strains plotted as a function of time.

loading cycle, the mechanical response, as shown in Figure 5e, is repeatable for the remaining cycles up to the maximum previous compressive strain with negligible hysteresis. Compared to a fully dense sample, the material exhibits a strong nonlinear response that increases sharply as the porous region is fully compressed. As shown in Figure S10 (Supporting Information), the effective elastic modulus of the sensor increased by more than 13× during deformation.

Multilayered dielectrics enable capacitive sensors to have a high sensitivity and a large dynamic range simultaneously.[58] Figure 5f shows the normalized change in capacitance as a function of cyclic loading at increasing levels of strain, from 10%, 20%, 30%, 40%, and 50%. The initial capacitance of the sensor was 15.0 pF. The response increases non-linearly as a function of compressive strain. There is notable hysteresis in the system, as the baseline capacitance almost doubles from 10 to 50% strain. This indicates that increasing compressive strain causes irreversible changes in the structure of the material. This is also illustrated in Figure 5g, where the baseline normalized capacitance increases with the maximum compressive strain. The response is observed to be repeatable after the first cycle up to the maximum previous compressive strain with negligible hysteresis.

For a parallel plate capacitor, the capacitance increases inversely proportional to the thickness (t) of the dielectric, $C = \epsilon_0 \epsilon_r A/t$, where $\epsilon_0 = 8.85 \times 10^{-12}$ is the vacuum permittivity, ϵ_r is the effective relative permittivity, and A is the planar area. As shown in Figure 5f, the large difference between the theoretical parallel plate model and the sensor response is due to the positive piezopermittivity of the foam structure. As the LM foam is compressed, the low ϵ_r air is displaced, resulting in ϵ_r increasing with compressive strain (Figure S11, Supporting Information). The gauge factor $((\Delta C/C_0)/(\Delta d/d_0))$ of the sensor ranges from 1.5 to 9 (Figure S12, Supporting Information). At 50% strain, the gauge factor of 9.0 is 800% higher than a fully dense sample, indicating high sensitivity and importance of the material structure.

These results are in good agreement with previous work[48] that created LM foam structures using sacrificial templates. The soft and highly sensitive capacitive sensor could be used in applications such as human-machine interaction, soft robotics, and electronic skins that require the ability to sense a wide range of pressures.

3. Conclusion

We have demonstrated the versatility of DIW 3D printing LM elastomer composites by fabricating both fully dense solids and functionally graded foams across a wide range of print velocities and heights. To achieve on-demand programming of LM droplet microstructure (i.e., shape and orientation), the printing process conditions are varied throughout the fabrication process, which directly influences the geometry of the filament and can lead to the formation of unintentional voids. Through systematic analysis of the interplay between the printing parameters and filament geometry, we determined optimal conditions for producing defect-free multilayered structures ranging from basic cubic forms to intricate interdigitated designs. We observed that beyond a certain print height threshold, the printed ink became discontinuous despite continuous nozzle movement. We exploit this instability and fracture behavior to create functionally graded foam structures with tailored porosity. By controlling the geometric structure and the LM microstructure, we demonstrated that the printed structures have improved thermal conductivity for passive thermal management, permittivity that increases with sensor strain for enhanced sensitivity, and reduced material density as compared to cast samples. These advancements in manufacturing, material properties, and performance provide opportunities for integration into diverse applications such as soft robotics, wearable electronics, and human-machine interfaces, including tactile sensors, soft energy harvesting devices, and passive heat spreaders. The combination of on-demand control of geometric structure and LM microstructure offers new opportunities for additive manufacturing and LM communities to create innovative materials, structures, and devices that possess a unique combination of functionalities.

4. Experimental Section

Liquid Metal Composite Fabrication: The LM composite ink was fabricated by dispersing LM microdroplets in a two-part polydimethylsiloxane (PDMS; ExSil 100; Gelest Inc.). The PDMS was first prepared by combining part A and part B at a 100:1 mass ratio and mixing in a planetary mixer (FlackTek SpeedMixer). The PDMS was then shear mixed at 800 rpm for 1 min with the LM at a high concentration ($\phi = 50\%$) and then loaded into a 10 mL syringe, creating microdroplets with 200 µm diameter.

Direct Ink Write 3D Printing: A Hyrel Engine SR 3D printer with a SDS-10 head was used to extrude the LM composite ink. A thin layer of Sylgard 184 (10:1 ratio) was cast on the aluminum bed to eliminate any defects on the print bed surface. The filaments were printed on a thin (125 µm) polycarbonate film (McMaster-Carr) adhered to the bed to facilitate easier removal and handling. When filaments were printed for analysis, a dark blue window tinting film was applied to the polycarbonate film surface to reduce noise during laser profilometry. Optimum SmoothFlow nozzles (Nordson EFD) with 0.58 mm diameter were used to extrude the ink.

Multilayer Printing: Multilayer structures were printed on a thin polycarbonate film (McMaster-Carr). Every other layer was partially cured using a heat gun set to 192 °C for 5 min, followed by cooling with a fan for 6 min. The heat gun was attached as a print head and controlled using a relay to automate the curing process. The cooling fan was rigidly attached to the print bed to increase cooling and controlled using a relay. Before starting a print and after every other layer was partially cured, a preextrusion line was deposited to ensure material flow reached a steady state prior to filament deposition. Multilayer structures printed at $V^* = 6$ and 12 consisted of 30 layers, whereas those printed at $V^* = 1$ were made of ten layers due to the larger filament size. $V^* = 6$ and 12 high AR structures were composed of 60 layers to make their height similar to that of $V^* = 1$ structures. ImageJ was used to determine the aspect ratio of interdigitated keys.

Laser Profilometry and Filament Geometry Analysis: The printed filaments were analyzed using a Keyence VK-X200K laser scanning microscope. A 20× lens was used to capture images and geometrical characteristics of each filament. For each combination of V^*, C, and H, three filaments with a 50 mm length in a serpentine pattern with 5 mm spacing were printed. $C = 6.8$ mm-s^{-1}, corresponded to $V = 6.8$, 40.8, and 81.6 mm-s^{-1} for $V^* = 1$, 6, and 12, respectively. $C = 5.0$ mm-s^{-1}, corresponded to $V = 5$, 30, and 60 mm-s^{-1} for $V^* = 1$, 6, and 12, respectively. $C = 2.5$ mm-s^{-1}, corresponded to $V = 2.5$, 15, and 30 mm-s^{-1} for $V^* = 1$, 6, and 12, respectively. It was noted that some of the combinations exceeded the recommended X/Y velocity of 30 mm-s^{-1}. The filament areas analyzed were randomly selected from the middle 30 mm section to account for possible velocity and height variations when the printer changed directions. The raw data was exported and processed in MATLAB. A symmetric moving average was applied to reduce noise in the data.

Porosity Analysis: A Nikon X-ray CT 225 ST was used to determine the porosity of the printed samples. The samples were mounted vertically on a custom base. The voxel dataset was acquired using 1,440 projections with two frames per projection. The data was processed in VGSTUDIO MAX (Volume Graphics).

Thermal Conductivity Demonstration: A Thermtest MP-V was used to perform transient plane source measurements for thermal conductivity. Cast samples were made by curing the LM composite or elastomer (ExSil 100, Gelest, Inc.) in molds for 24 h at 50 °C. A sensor with a radius of 9.9 mm was placed between two homogenous samples. The sample was placed between two silicone slabs on top of the sample stand. An acrylic sheet and 500 g mass were then placed on top of the silicone to ensure good contact between the sensor and the material. The samples were measured using the "Symmetric", "Slab", and "Isotropic" strategies. Measurements were taken at 20 °C for 20 s for each sample except for the cast LM composite, which was tested for 3 s. The power used for the fully dense $V^* = 12$ sample, porous $V^* = 12$ sample, cast LM composite, and elastomer were 408, 204, 302, and 87 mW, respectively.

Mechanical and Electrical Characterization of LM Foam: An Instron mechanical testing machine (5966) was used to conduct compressive tests on the sample. Two 30 x 30 mm sheets of copper tape were used as electrodes and applied to the top and bottom of the LM elastomer composite foam gradient. Additional copper tape was attached to the electrodes as leads for the digital multimeter (Keithley DMM6500, Tektronix). The foam gradient and electrodes were placed between two slabs of acrylic for uniform compression. The Instron was equipped with a 2 kN load cell.

Supporting Information

Supporting Information is available from the Wiley Online Library or from the author.

Acknowledgements

S.P. and E.M. acknowledged support through (No. CMMI-2054411), NASA Nebraska EPSCoR (80NSSC19M0065), and the Nebraska Tobacco Settlement Biomedical Research Development Fund. M.B. acknowledged support through NSF (No. CMMI-2054409). Manufacturing and characterization analysis were performed at the NanoEngineering Research Core Facility, National Nanotechnology Coordinated Infrastructure, and the Nebraska Center for Materials and Nanoscience, which were supported by

the National Science Foundation under Award ECCS: 1542182, and the Nebraska Research Initiative.

Conflict of Interest

The authors declare no conflict of interest.

Data Availability Statement

The data that support the findings of this study are available from the corresponding author upon reasonable request.

Keywords

3D printing, additive manufacturing, liquid metal, microstructure, soft robots

Received: June 21, 2024
Revised: August 12, 2024
Published online:

[1] R. L. Truby, J. A. Lewis, *Nature* **2016**, *540*, 371.
[2] M. Saadi, A. Maguire, N. T. Pottackal, M. S. H. Thakur, M. M. Ikram, A. J. Hart, P. M. Ajayan, M. M. Rahman, *Adv. Mater.* **2022**, *34*, 2108855.
[3] A. Haake, R. Tutika, G. M. Schloer, M. D. Bartlett, E. J. Markvicka, *Adv. Mater.* **2022**, *34*, 2200182.
[4] O. Hur, R. Tutika, N. Klemba, E. J. Markvicka, M. D. Bartlett, *Addit. Manuf.* **2023**, *79*, 103925.
[5] J. Wang, G. Cai, S. Li, D. Gao, J. Xiong, P. S. Lee, *Adv. Mater.* **2018**, *30*, 1706157.
[6] T. V. Neumann, E. G. Facchine, B. Leonardo, S. Khan, M. D. Dickey, *Soft Matter* **2020**, *16*, 6608.
[7] R. Tandel, B. A. Gozen, *J. Mater. Process. Technol.* **2021**, *302*, 117470.
[8] Y. Han, L.-E. Simonsen, M. H. Malakooti, *Adv. Energy Mater.* **2022**, *12*, 2201413.
[9] W. Zu, Y. Ohm, M. R. Carneiro, M. Vinciguerra, M. Tavakoli, C. Majidi, *Adv. Mater. Technol.* **2022**, *7*, 2200534.
[10] M. A. Skylar-Scott, J. Mueller, C. W. Visser, J. A. Lewis, *Nature* **2019**, *575*, 330.
[11] H. Yuk, X. Zhao, *Adv. Mater.* **2018**, *30*, 1704028.
[12] S. Abdollahi, E. J. Markvicka, C. Majidi, A. W. Feinberg, *Adv. Healthcare Mater.* **2020**, *9*, 1901735.
[13] S. Jang, A. Boddorff, D. J. Jang, J. Lloyd, K. Wagner, N. Thadhani, B. Brettmann, *Addit. Manuf.* **2021**, *47*, 102313.
[14] R. Tandel, B. A. Gozen, *J. Mater. Process. Technol.* **2022**, *302*, 117470.
[15] A. Kotikian, R. L. Truby, J. W. Boley, T. J. White, J. A. Lewis, *Adv. Mater.* **2018**, *30*, 1706164.
[16] S. Gantenbein, K. Masania, W. Woigk, J. P. Sesseg, T. A. Tervoort, A. R. Studart, *Nature* **2018**, *561*, 226.
[17] D. J. Roach, X. Kuang, C. Yuan, K. Chen, H. J. Qi, *Smart Mater. Struct.* **2018**, *27*, 125011.
[18] C. P. Ambulo, J. J. Burroughs, J. M. Boothby, H. Kim, M. R. Shankar, T. H. Ware, *ACS Appl. Mater. Interfaces* **2017**, *9*, 37332.
[19] B. G. Compton, J. A. Lewis, *Adv. Mater.* **2014**, *26*, 5930.
[20] H. L. Tekinalp, V. Kunc, G. M. Velez-Garcia, C. E. Duty, L. J. Love, A. K. Naskar, C. A. Blue, S. Ozcan, *Compos. Sci. Technol.* **2014**, *105*, 144.
[21] H. Jeong, *J. Compos. Mater.* **1997**, *31*, 276.
[22] A. Chambers, J. Earl, C. Squires, M. Suhot, *Int. J. Fatigue* **2006**, *28*, 1389.
[23] A. Hernandez-Contreras, L. Ruiz-Huerta, A. Caballero-Ruiz, V. Moock, H. R. Siller, *Materials* **2020**, *13*, 3831.
[24] R. Tutika, S. H. Zhou, R. E. Napolitano, M. D. Bartlett, *Adv. Funct. Mater.* **2018**, *28*, 1804336.
[25] M. I. Ralphs, N. Kemme, P. B. Vartak, E. Joseph, S. Tipnis, S. Turnage, K. N. Solanki, R. Y. Wang, K. Rykaczewski, *ACS Appl. Mater. Interfaces* **2018**, *10*, 2083.
[26] E. J. Krings, H. Zhang, S. Sarin, J. E. Shield, S. Ryu, E. J. Markvicka, *Small* **2021**, *17*, 2104762.
[27] A. T. Haque, R. Tutika, R. L. Byrum, M. D. Bartlett, *Adv. Funct. Mater.* **2020**, *30*, 2000832.
[28] R. Herbert, P. Mocny, Y. Zhao, T.-C. Lin, J. Zhang, M. Vinciguerra, S. Surprenant, W. Y. D. Chan, S. Kumar, M. R. Bockstaller, K. Matyjaszewski, C. Majidi, *Adv. Funct. Mater.* **2023**, *34*, 2309725.
[29] E. J. Markvicka, M. D. Bartlett, X. Huang, C. Majidi, *Nat. Mater.* **2018**, *17*, 618.
[30] W. Zu, H. E. Carranza, M. D. Bartlett, *ACS Appl. Mater. Interfaces* **2024**, *16*, 23895.
[31] R. Tutika, A. T. Haque, M. D. Bartlett, *Commun. Mater.* **2021**, *2*, 64.
[32] A. T. Haque, D. H. Ho, D. Hwang, R. Tutika, C. Lee, M. D. Bartlett, *Adv. Funct. Mater.* **2023**, *34*, 2304101.
[33] C. J. Thrasher, Z. J. Farrell, N. J. Morris, C. L. Willey, C. E. Tabor, *Adv. Mater.* **2019**, *31*, 1903864.
[34] S. Liu, D. S. Shah, R. Kramer-Bottiglio, *Nat. Mater.* **2021**, *20*, 851.
[35] R. Tutika, S. Kmiec, A. T. Haque, S. W. Martin, M. D. Bartlett, *ACS Appl. Mater. Interfaces* **2019**, *11*, 17873.
[36] C. Pan, E. J. Markvicka, M. H. Malakooti, J. Yan, L. Hu, K. Matyjaszewski, C. Majidi, *Adv. Mater.* **2019**, *31*, 1900663.
[37] M. D. Bartlett, A. Fassler, N. Kazem, E. J. Markvicka, P. Mandal, C. Majidi, *Adv. Mater.* **2016**, *28*, 3726.
[38] E. J. Krings, B. D. Hage, S. L. Truong, K. A. Reeser, E. L. Fox, M. G. Snyder, Q. Walker, G. R. Bashford, E. J. Markvicka, *Adv. Funct. Mater.* **2023**, *34*, 2308954.
[39] J. W. Kopatz, D. Reinholtz, A. W. Cook, A. S. Tappan, A. M. Grillet, *Addit. Manuf.* **2024**, *80*, 103928.
[40] A. B. Chu, M. Murialdo, J. P. Lewicki, J. N. Rodriguez, M. K. Shiflett, B. Giera, A. D. Kaplan, in *2019 18th IEEE International Conference On Machine Learning And Applications (ICMLA)*, IEEE, Piscataway, NJ **2019**, pp. 1342–1347.
[41] D. J. Kline, M. D. Grapes, R. C. Morales, G. C. Egan, J. D. Sain, Z. D. Doorenbos, H. E. Fletcher, E. A. Avalos, B. M. English, V. Eliasson, K. T. Sullivan, J. L. Belof, *Addit. Manuf.* **2022**, *56*, 102896.
[42] N. Petchwattana, S. Covavisaruch, *Mater. Des.* **2011**, *32*, 2844.
[43] H. Wang, R. Zhang, D. Yuan, S. Xu, L. Wang, *Adv. Funct. Mater.* **2020**, *30*, 2003995.
[44] D. Klempner, *Handbook of Polymeric Foams and Foam Technology*, Hanser, Munich, Germany **1991**.
[45] L. J. Jacobs, M. F. Kemmere, J. T. Keurentjes, *Green Chem.* **2008**, *10*, 731.
[46] J. T. Muth, P. G. Dixon, L. Woish, L. J. Gibson, J. A. Lewis, *Proc. Natl. Acad. Sci.* **2017**, *114*, 1832.
[47] L. M. Matuana, C. A. Diaz, *Ind. Eng. Chem. Res.* **2010**, *49*, 2186.
[48] J. Yang, D. Tang, J. Ao, T. Ghosh, T. V. Neumann, D. Zhang, Y. Piskarev, T. Yu, V. K. Truong, K. Xie, Y.-C. Lai, Y. Li, M. D. Dickey, *Adv. Funct. Mater.* **2020**, *30*, 2002611.
[49] X. Mu, T. Bertron, C. Dunn, H. Qiao, J. Wu, Z. Zhao, C. Saldana, H. Qi, *Mater. Horiz.* **2017**, *4*, 442.
[50] D. Wu, F. Xu, B. Sun, R. Fu, H. He, K. Matyjaszewski, *Chem. Rev.* **2012**, *112*, 3959.
[51] M. Costantini, J. Jaroszewicz, Ł. Kozoń, K. Szlązak, W. Święszkowski, P. Garstecki, C. Stubenrauch, A. Barbetta, J. Guzowski, *Angew. Chem., Int. Ed.* **2019**, *58*, 7620.
[52] J. Elsing, A. Quell, C. Stubenrauch, *Adv. Eng. Mater.* **2017**, *19*, 1700195.

[53] C. W. Visser, D. N. Amato, J. Mueller, J. A. Lewis, *Adv. Mater.* **2019**, *31*, 1904668.
[54] R. G. Larson, P. S. Desai, *Annu. Rev. Fluid Mech.* **2015**, *47*, 47.
[55] J. Wang, L. L. Shaw, *Mater. Sci. Eng., A* **2005**, *397*, 314.
[56] P.-T. Brun, B. Audoly, N. M. Ribe, T. S. Eaves, J. R. Lister, *Phys. Rev. Lett.* **2015**, *114*, 174501.
[57] M. K. Jawed, P.-T. Brun, P. M. Reis, *J. Appl. Mech.* **2015**, *82*, 121007.
[58] J. Yang, K. Y. Kwon, S. Kanetkar, R. Xing, P. Nithyanandam, Y. Li, W. Jung, W. Gong, M. Tuman, Q. Shen, M. Wang, T. Ghosh, K. Chatterjee, X. Wang, D. Zhang, T.-i. Kim, V. T. Khanh, M. D. Dickey, *Adv. Mater. Technol.* **2022**, *7*, 2101074.